Chapter 7
Convective Heat Transfer in a Pipe Rotating Around a Parallel Axis

7.1 Experiments and Simulations of Different Authors

Introduction. Rotors of electrical machines used in railway transport, electric generators, etc., are subject to internal heating due to high electromagnetic losses. This involves installation of internal air cooling systems incorporating rotating straight pipes [1–4]. This chapter is based on the results of the CFD simulations of such a cooling geometry published in [5]. Cross sections of the studied electric motor and respective CFD model are schematically depicted in Fig. 7.1.

Channels of an air cooling configuration are uniformly installed along the circumference inside the rotor (see Fig. 7.1a, b). Rotation of the pipes causes secondary flows, which are absent in non-rotating channels, provided that the inlet and thermal boundary conditions are the same. Consequently, heat transfer and hydraulic resistance cannot be predicted with the help of standard correlations used for non-rotating pipes.

The geometrical configuration employed in [5] is shown in Fig. 7.1c. In channels rotating parallel to the rotation axis, centrifugal buoyancy, and Coriolis forces emerge [1, 3, 4, 6]. The Coriolis force is defined as a vector product of the absolute flow velocity and the angular velocity of a rotating channel [3, 6, 7]. Non-collinear vectors result in nonzero Coriolis forces, whose absolute value is defined by the magnitudes of the flow velocity and angular velocity vectors, as well as angles between them [3, 6, 7]. If flow develops through the entrance hydrodynamic length of a pipe, velocity profiles are non-stabilized with rather high-velocity components perpendicular to the vector of the angular velocity (and channel walls) resulting in rather high Coriolis forces. In case where centrifugal buoyancy is negligible and channel flow attains a fully hydrodynamically developed state, the streamwise velocity component by far surpasses the radial and tangential components. Thus, the axial and angular velocity vectors become collinear (Fig. 7.1c), whereas the Coriolis force defined by their vector product tends to zero. An account for centrifugal buoyancy is needed, if centrifugal acceleration and wall heat flux are

I.V. Shevchuk, *Modelling of Convective Heat and Mass Transfer in Rotating Flows*, Mathematical Engineering, DOI 10.1007/978-3-319-20961-6_7

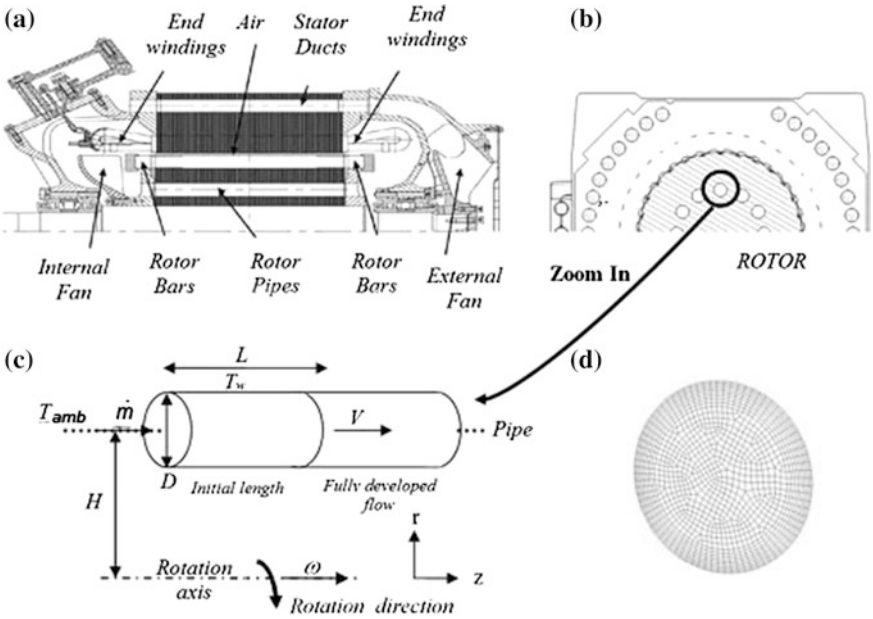

Fig. 7.1 Studied electrical motor: **a** side view; **b** front view; **c** schematic representation of the problem; **d** mesh at the inlet surface [5]

sufficiently large to cause macro-vortex flow occupying the entire channel cross section, with Coriolis forces only distorting the main secondary flow.

Rotation effects in the considered configuration are described by four similarity criteria: (1) Rossby number $Ro = \omega D/\bar{V}$, a ratio of the Coriolis forces (manifested by the angular velocity ω) to inertia forces (represented by the average streamwise flow velocity in the channel $\bar{V}$), while a characteristic length is the pipe diameter D; (2) rotational Reynolds number $Re_\omega = \omega D_h^2/\nu$; (3) eccentricity parameter H/D_h; and (4) Rayleigh number $Ra_H = \omega^2 H^3 D_h \beta \Delta T/(2\lambda\nu)$ that stands for centrifugal buoyancy. Channel cross section (circular, square, rectangular, or elliptic) also makes a noticeable influence on fluid flow and heat transfer [3, 5–15]. For relatively low Rayleigh numbers, buoyancy effects were vanishingly small. The coolant in experiments considered in this chapter was air.

Circular pipes. In the work [6], heat transfer in turbulent flow over the initial length of the pipe was investigated at ω = 280–2200 rpm and Re = 5000–20,000. Experiments demonstrated that the local Nusselt number increased with increasing $\omega^2 H$.

Experimental data [14] collapsed to an empirical relation (scatter ±14 %)

$$\overline{Nu} = 0.19 Re^{0.56} Re_\omega^{0.1}, \tag{7.1}$$

where L/D = 19.3, H/D = 25.19, Re = 5500–33,000, Re_ω = 600–4000, $Ro \le 0.75$, and ω = 280–2200 rpm. In the non-rotating pipe of the same geometry [14], obtained that $\overline{Nu}_0 = 0.031Re^{0.79}$, which together with Eq. (7.1) yields [3]

$$\overline{Nu}/\overline{Nu}_0 = 6.129Re^{-0.23}Re_\omega^{0.11}. \tag{7.2}$$

Experiments [12] were described by an equation (scatter ±12 %)

$$\overline{Nu} = 0.015Re^{0.78}(Re_\omega/8)^m, \tag{7.3}$$

with m = 0.25. However, authors [3] revealed that an exponent m = 0.2 ensures better agreement with experiments [12]. Here, H/D = 24.02, L/D = 36.65 or H/D = 48.03, L/D = 69.03, Re = 5000–20,000, and Re_ω = 120–1200 (ω = 0–1000 rpm) with $Ro \le 0.14$.

Experimental data [9] were approximated by an empirical equation

$$\overline{Nu} = 0.018Re^{0.8}(1 - 2D/L)\,(1 + 0.6RoH/D), \tag{7.4}$$

with H/D = 23.3, $Re = (1–4.8) \times 10^4$, $RoH/D \le 1.6$, $Ro \le 0.07$, ωH = 0–30 m/s, and ω = 0–18.33 s^{-1}.

Equations (7.2) and (7.3) for $Ro \le 0.14$ were generalized in the following form [3]

$$\overline{Nu} = \overline{Nu}_0(1 + 28Ro)^{0.5}. \tag{7.5}$$

Experiments of Baudoin [8] yield the following empirical equations

$$\overline{Nu}/\overline{Nu}_0 = 1 + 0.46(RoH/D)^{1.24}, \tag{7.6}$$

$$\overline{Nu}_0 = 0.023Pr^{1/3}Re^{0.8}\left(1 + (D/L)^{0.7}\right), \tag{7.7}$$

where H/D = 3, L/D = 11.6, Re = 3000–25,000, ω = 0–150 s^{-1}, and $T_{ref} = (T_i + T_{m-out})/2$. With a 14 % increase in the eccentricity, heat transfer increased in experiments by 7 % [8].

Square, rectangular, and elliptic pipes. In [13], experiments have been performed in a square channel, which were described by an empirical equation (scatter ±14 %)

$$\overline{Nu} = 0.011Re^{0.78}Re_\omega^{0.11}, \tag{7.8}$$

where L/D_h = 48, H/D_h = 32–48, Re_ω = 100–1000, and $Re \le 2500$. Equation (7.8) predicts noticeably lower heat transfer rates than the one in a circular pipe, Eq. (7.3) [12]. The exponent 0.78 for the Reynolds number in the range Re = 100–1000 is an evidence of an earlier transition to turbulence excited by the rotation effects.

Eccentricity effect was studied experimentally by Mori et al. [11] in a rectangular channel. Eccentricity was equal to 6 in a fully heated channel and to 30 or 60 in a channel with only a half cross section heated. Angular velocity was set to vary from 800 to 3000 rpm. At the eccentricity parameter equal to 6, Mori et al. [11] obtained an empirical equation for the mean Nusselt number

$$\overline{Nu} = 2.1 Re_{\omega}^{0.11} \left[Re (D_{\mathrm{h}}/L)^{1.6} \right]^{0.43} Ra_H^{0.021}, \tag{7.9}$$

where Re = 2000–10,000 and $Ra_H = 10^8$–2.0×10^{10}. The effect of the centrifugal buoyancy was very weak. Mori et al. [11] assert that Eq. (7.9) agrees well with experiments [6].

The 3D fluid flow and heat transfer were numerically modeled in the works of [1, 4, 6, 10, 15] in channels with circular, square, rectangular, and elliptic cross sections with the help of different CFD codes and RANS turbulence models. In simulations of Mahadevappa et al. [10], the highest heat transfer enhancement was attained in circular pipes, while elliptic channels are in an intermediate standing between circular and rectangular channels.

To conclude, the empirical equations considered above quite noticeably disagree with each other. The effect of the eccentricity parameter H/D was considered only in the works of [8, 9], where values of H/D were very different, H/D = 23.3 in [9] and H/D = 3 in [8]. Maximal angular velocity $\omega = 18.33\ \mathrm{s}^{-1}$ in [9] was by a factor of 8 smaller than $\omega = 150\ \mathrm{s}^{-1}$ in [8]. To compare, maximal angular velocity was $50\ \mathrm{s}^{-1}$ in [15] and much lower in the rest of the referenced works. Thus, the only experiments [8] were performed under conditions close to those studied in our CFD investigation [5]. Also, perspectives of heat transfer enhancement at the expense of morphing of the pipe cross section to fit into a real electrical motor remained not elucidated.

Therefore, the *objective* of the study presented here was to use the CFD methodology to investigate the effects of the pipe cross-sectional design on the convective heat transfer in airflow in the channels rotating parallel to a rotation axis. Two types of pipes were studied having an elliptic cross section located radially or circumferentially with respect to the rotation radius. A separate study was performed on the effect of the flow angle of attack at the pipe inlet never investigated in the published literature. Experiments of Baudoin [8] were employed to validate the results of the numerical simulations.

7.2 Computational Model

Dimensions of the circular or elliptic pipe depicted in Fig. 7.1c are similar to a real design of a railway transportation motor [5]. Air is fed into the pipe at a given mass flow rate $\dot{m}$ and inlet temperature $T_{\mathrm{i}} < T_w$ (T_{i} is equal to the ambient temperature). The distance between the rotation and the pipe axes stands for the eccentricity, denoted as H.

7.2.1 Simulation Parameters

The pipe geometry was meshed using the preprocessor GAMBIT. The volume mesh incorporated a 10-cell prism layer at the pipe wall, quad surface cells outside of the boundary layer (Fig. 7.1d), and hexahedral cells forming the volume mesh. Having validated four different volume meshes of 100,000–500,000 elements by way of simulating the average surface heat transfer, it was proved that mesh independence was attained with the mesh size of about 350,000 elements, consisting of 250 cells in the axial, 17 cells in the radial, and 80 cells in the tangential (angular) direction.

In case if the interaction between stationary and rotating parts of geometry is weak, it is suggested by FLUENT [16] to use a rotating reference frame approach. In the new frame, the pipe becomes non-rotating, while Coriolis and centrifugal terms emerge explicitly in the Navier–Stokes equations. This approach was used in the present work.

Turbulence properties were constant at the inlet cross section and set to 10 % for turbulence intensity and 10 for the turbulent viscosity ratio (see definitions in [16]). These values were suggested by previous simulations of the entire motor [5]. Lower levels of the turbulence properties cause underestimated values of the Nusselt number.

The air temperature T_{i} at the inlet to the pipe and the wall temperature T_w were constant: $T_{\mathrm{i}} = 323$ K and $T_w = 473$ K. The mass flow rate $\dot{m}$ was chosen based on the measured data for a real engine (see below). Flow velocity at the inlet was mostly normal to the inlet face. A non-normal inlet velocity was assigned while investigating effects of the angle of attack. The range of variation of the angular velocity of rotation was $0 \le \omega \le 145\ \mathrm{s}^{-1}$.

Magnetic flux in the electric motor exhibits a strongly non-uniform 3D distribution that results in a nonuniform surface distribution of the heat flux per unit area q_w in the cooling channels. If the longitudinal distribution of the wall temperature T_w in straight channels used in the air cooling systems is moderately different from the condition $T_w = \mathrm{const.}$, the cross-sectional averaged Nusselt number is close to that for $T_w = \mathrm{const.}$ (see, e.g., [17]). This phenomenon is widely used both in experimental measurements of the local Nu numbers by means of TLCs at arbitrary variation of the local surface temperature (see [18, 19]) and in the CFD or analytical modeling of heat transfer at the boundary condition $T_w = \mathrm{const.}$ (see [18, 20]).

Rayleigh numbers were estimated as $Ra_H = 2 \times 10^8$, which in view of the Reynolds number $Re = 3500$ in the present investigation delivers conditions with vanishingly small centrifugal buoyancy effects [7, 11].

At the pipe outlet, a boundary condition of mass flow conservation was assigned.

7.2.2 Choice and Validation of the Turbulence Model

Five different turbulence models implemented in FLUENT were investigated in the present study:

Table 7.1 Geometrical setup in the benchmark experiments and the validation tests [5]

	Baudoin [8]	Present configuration
D (mm)	24	25
H (mm)	72	82.5
L (mm)	280	285
$\dot{m}$ (kg/s)	0.006	0.0066
ω s^{-1}	0–150	0–145
L/D	11.66	11.4
H/D	3	3.3

- k-ε model with an *enhanced wall treatment*,
- k-ε RNG model with an *enhanced wall treatment*,
- realizable k-ε model with an *enhanced wall treatment*,
- standard k-ω model, and
- k-ω SST model.

All five models require a mesh with the first mesh point very close to the wall ($y+ \sim 1$). The mesh with 350,000 elements resulted in the wall values $0.5 \leq y+ \leq 5$ for all turbulence models [5].

The geometry used for the turbulence model testing was close to that used by Baudoin [8]. Geometrical parameters, mass flow rate, and angular velocity of rotation for our and Baudoin's [8] configurations are specified in Table 7.1.

In our simulations [5], Ro number varied from 0.008 to 0.35 at Re = 14,000. Calculations in order to select an appropriate turbulence model were made at Ro = 0.088. In Table 7.2, the mean Nusselt numbers obtained from the simulations are compared with the value 56.4 from Baudoin's Eq. (7.6). The best agreement delivered the standard k–ω turbulence model with a relative error not exceeding 10 %. Use of the rest of the models entailed much more significant deviations from experiments (up to 60 % in the worst case). Hence, the standard k–ω turbulence model was selected for further simulations.

As seen from Fig. 7.2, simulations based on the standard k–ω turbulence model correlate well with Baudoin's empirical Eq. (7.6) [8]. This enabled further use of the developed CFD model in simulations of the effects of the pipe geometry and inlet boundary conditions stated above in the objectives of the present research.

Table 7.2 Mean Nusselt numbers in simulations [5] and experiments [8] for the circular pipe

	Nu	Difference (%)
Baudoin [8]	56.4	–
k-ε standard	90.9	60.6
k-ε RNG	86.8	53.9
k-ε realizable	80.2	42.2
k-ω standard	51.8	−8.2
k-ω SST	66.1	17.2

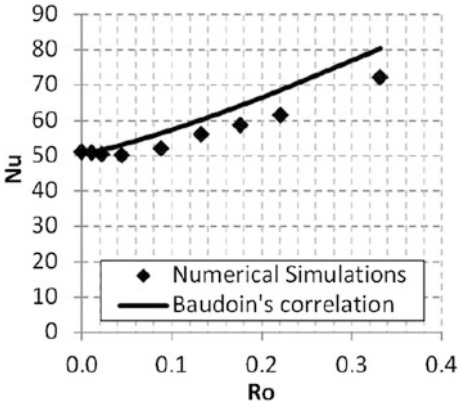

Fig. 7.2 Mean Nusselt numbers versus the Rossby number, simulations using the standard k–ω model (*points*) and Baudoin's empirical Eqs. (7.6) and (7.7) (*line*) [5]

7.3 Circular Pipe: Effect of the Angle of Attack

Parameters of the model. The circular pipe involved in Sect. 7.2.2 in the simulations (see Table 7.1) was employed also here as a reference pipe at Re = 3500 and Ro = 2.24. This value of the Re number can be recalculated to a total mass flow rate of $\dot{m} = 0.018$ kg/s in 12 pipes with D = 0.025 m (i.e., $\dot{m} = 0.0015$ kg/s in each pipe) and an angular velocity of 2200 rpm chosen in conformance with specifications for an industrial motor prototype. Temperature boundary conditions were T_i = 323 K and T_w = 473 K. Results for the reference case (velocity profile orthogonal to the inlet) were juxtaposed against simulations of the cases with different flow angle of attack or morphed cross-sectional shape.

Different angles of attack. This part of the study elucidates the effects of different inlet velocity profiles (Fig. 7.3) at the same total mass flow rate for all studied cases.

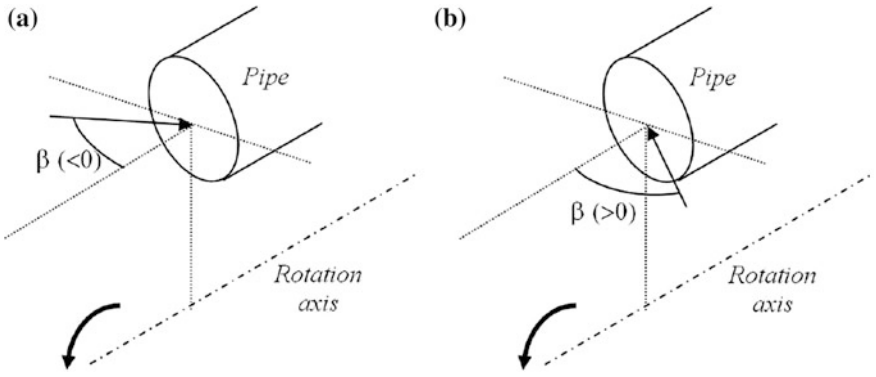

Fig. 7.3 Definition of the angle of attack; **a** negative angles; **b** positive angles [5]

If the velocity of rotation of air is smaller than that of the pipes, the flow angle of attack at the inlet is negative (Fig. 7.3). Axial v_z and tangential v_φ velocity components of the airflow in the simulations were constant at the inlet cross section, with the angle of attack β defined as $v_\varphi = v_z \tan(\beta)$, $v_z = 4\dot{m}/\rho\pi D^2$. Six different angles of attack were used: −80°, −58°, −28°, 28°, 58°, and 80°. An angle of 0° means an orthogonally entering flow. Negative angles denote that the flow at the inlet is contra-rotating with respect to the pipe.

Consequently, the axial velocity component at pipe inlet was calculated as $v_z/(\omega H) = 0.134$, while the resulting velocity $V_{\text{tot}} = \sqrt{v_z^2 + v_\varphi^2} = v_z\sqrt{1 + \tan^2\beta}$ varied over the range $V_{\text{tot}} = 2.54{-}14.63$ m s^{-1}.

If an electrical motor is rotating, airflow fed to the cooling system is non-orthogonal to the inlet of the rotating channels. The flow angle of attack (i.e., the shape of the velocity profile) influences the heat transfer inside the pipe either enhancing or suppressing it.

Table 7.3 represents a comparison of the mean Nusselt numbers predicted for the conditions with different inlet velocity profiles. As seen from Table 7.3, heat transfer is enhanced only if the air at the inlet to the pipe is contra-rotating with respect to the pipe wall (negative angle of attack). An increase in the mean Nusselt numbers reached 31 % for the largest negative angle of attack −80°. When the incoming flow and the pipe were corotating, mean heat transfer reduced in comparison with the reference case of β = 0°.

Figure 7.4a depicts the local cross-sectional averaged Nusselt numbers as a function of the axial coordinate $z^* = z/D_h$ in the rotating pipe (for the highest and lowest angle of attack) and the stationary reference pipe. Variation of turbulence intensity (also cross section averaged) in the streamwise direction is outlined in Fig. 7.4b. Figure 7.4c represents results for the relative Nusselt number $(Nu - Nu_{\text{ref}})/Nu_{\text{ref}}$ for both angles of attack.

Turbulence intensity and local Nusselt numbers demonstrate similar trends: Plotted against the reference case of β = 0°, they are augmented at negative and decreased at positive angles of attack β (see Fig. 7.4). For the positive value β = 80°, the local Nusselt number at $z^* > 1$ demonstrates a rather weak variation, which differs from the curves for the other values of β. For the negative angle β = −80° at z^* = 0–3.6 (initial hydrodynamic length), the Nusselt number is high and goes beyond the stabilized value by up to 100 %.

Table 7.3 Influence of the angle of attack on mean heat transfer in the circular pipe [5]

Angle β	Nu	Difference (%)
−80°	53.1	31.1
−58°	45.8	13.1
−28°	43.7	7.9
Reference case 0°	40.5	–
28°	39.3	−2.9
58°	38.1	−5.9
80°	29.3	−27.7

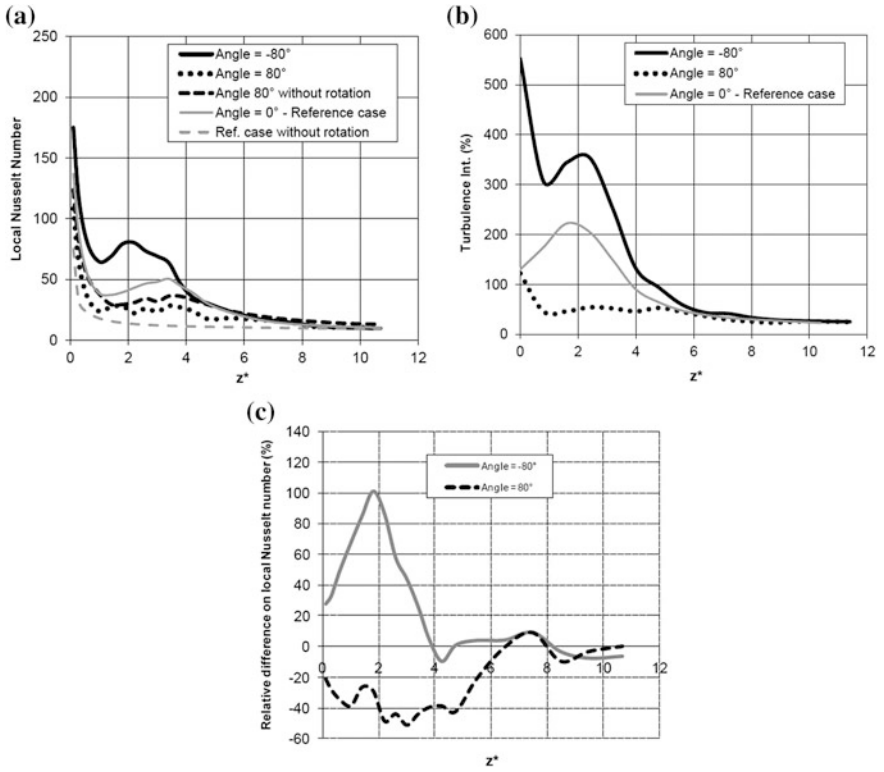

Fig. 7.4 Effect of the angle of attack: **a** local Nusselt number; **b** turbulence intensity; **c** relative difference of the Nusselt number with the reference case [5]

For all angles of attack, the Nusselt number noticeably decreased and reached for $z^* > 6$ nearly constant values of about 10–12. The FLUENT code predicts the Nusselt number $Nu_0 = 9.5$ at the end of a non-rotating pipe (zero rotation reference case in Fig. 7.4a). One can conclude from here that rotation still causes a weak effect on convective heat transfer at the end of the rotating pipe, whose length is insufficient to ensure independency of the local Nusselt number from rotation, which is otherwise expected to collapse to the non-rotating pipe value $Nu_0 = 9.5$. Dittus-Boelter equation for the developed flow in a non-rotating pipe [21]

$$Nu_0 = 0.023 Re^{0.8} Pr^{0.4} \tag{7.10}$$

predicts the value $Nu_0 = 14$, which is about 47 % higher than $Nu_0 = 9.5$ by FLUENT. Authors [20] also noticed that the Nusselt number resulting from the simulations with the help of FLUENT is smaller than those predicted by Eq. (7.10).

As seen from Fig. 7.4, once the flow reaches a certain axial location z^*, it turns to be *quasi-stabilized*, i.e., independent of the inlet velocity profile, with all the curves

asymptotically tending to a constant level lying still above the correspondent values for a non-rotating pipe for identical *Re* numbers.

Quasi-stabilized flow with zero angle of attack at the inlet is subject to internal swirl in the end of the pipe (see Fig. 7.5) that is apparently the reason for the Nusselt number to surpass its benchmark value in the reference non-rotating pipe.

Only the initial length of the pipe is subject to tangible effects of rotation. Figure 7.4b reveals high turbulence intensity levels for the negative angle $\beta = -80°$ right after the inlet to the pipe. The reason for this phenomenon is strong shear stresses engendered by collision of the flow and the pipe wall due to their contra-rotation at the pipe inlet.

Having passed the location $z^* = 6$, the flow turns to be quasi-stabilized and attains practically the same turbulence intensity levels for all cases depicted in Fig. 7.4b. This testifies that the Rayleigh number (i.e., centrifugal buoyancy) has no effect on convective heat transfer in the rotating pipe considered in the present work.

Figure 7.6 depicts perspective and longitudinal views of the surface heat flux distributions in the pipe for the reference and extreme cases of $\beta = 80°$ and $-80°$. As seen from Fig. 7.6, the heat transfer enhancement next to the inlet of the pipe lies behind the overall heat transfer enhancement in the pipe. This conclusion conforms to [6, 12], who believed that namely the flow pattern immediately downstream of the pipe inlet determines overall peculiarities of convective heat transfer in the pipe. The effect of the angle of attack on heat transfer in comparison with the reference case exhibits itself only next to the pipe inlet, where local heat transfer rates are highest.

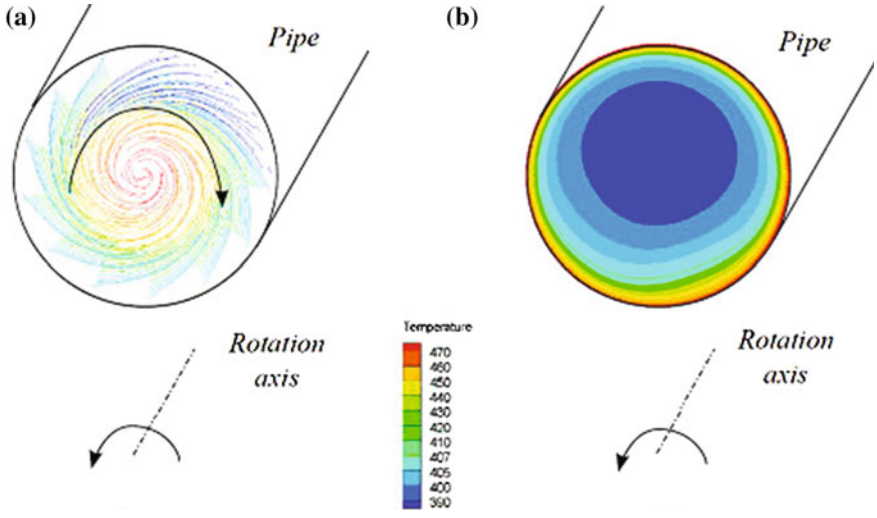

Fig. 7.5 Flow at the outlet of the rotating circular pipe with $\beta = 0°$ (reference case): **a** quasi-stabilized swirling flow, **b** temperature distribution [5]

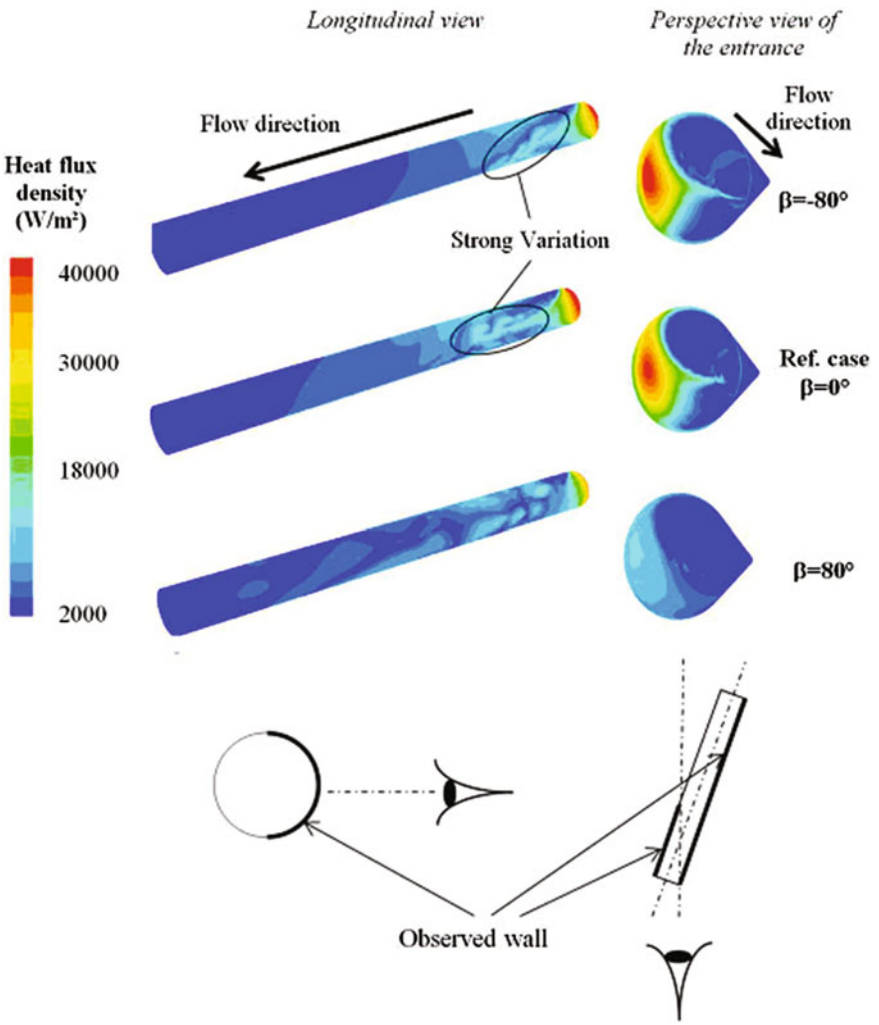

Fig. 7.6 Influence of the angle of attack on the local surface heat transfer [5]

Strong variation of the local surface heat transfer seen in the cases with $\beta = -80°$ and 0° disappears in the case with $\beta = 80°$ representing the worst cooling case (Fig. 7.6).

Positive angle of attack β (corotating flow and pipe wall) entails noticeable diminution of the local heat transfer next to the pipe inlet, because of the much weaker flow impingement onto the pipe wall. The difference in the circumferential velocities of the air and pipe wall next to the inlet is rather small, which causes small shear stresses and heat transfer on the pipe wall. On the contrary, a negative angle of attack β (contra-rotating flow and pipe wall) causes stronger air impingement onto the pipe wall and higher heat transfer.

To conclude, the efficiency of the pipe cooling is significantly affected by the angle of attack of the flow fed into the pipe. The incoming flow and the pipe itself must be contra-rotating to boost the impingement effects that entail shear stress and heat transfer augmentation next to the pipe inlet. In doing so, heat transfer enhances by 30 % at the largest angle of attack of $\beta = -80°$ of those studied in this work. In practice, contra-rotation of flow and pipe at the inlet can be ensured via installing flow deflectors.

7.4 Elliptic Pipe

Convective heat transfer in a cooling system can be enhanced by replacing the circular cross section of the pipe with an elliptic one. Elliptic cross section was positioned circumferentially or radially, i.e., perpendicular or aligned with the rotation radius (Fig. 7.7), with the hydraulic or equivalent diameter of the pipe retained unchanged.

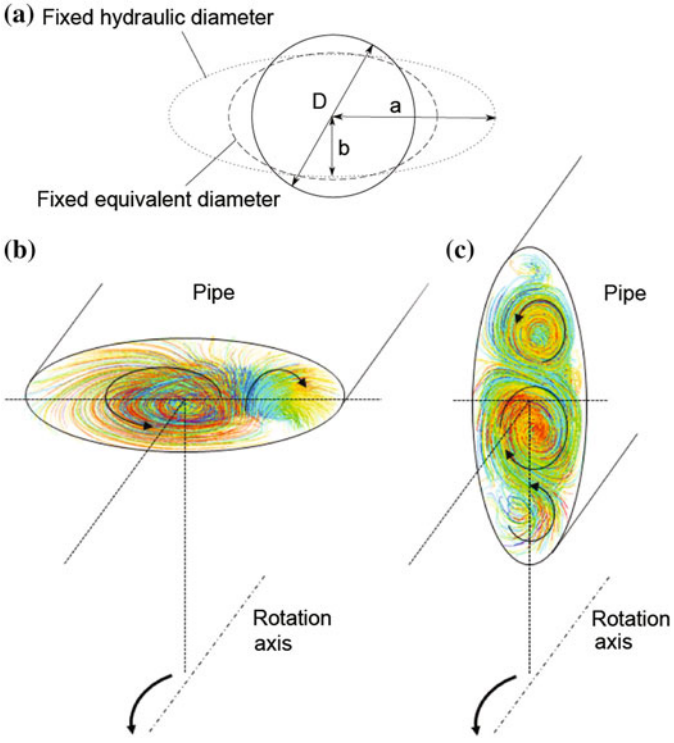

Fig. 7.7 Schematics of the circular and both elliptic cross sections (**a**); path lines at the pipe outlet of elliptic pipes with the fixed hydraulic diameter for the circumferential pipe (**b**) and radial pipe (**c**) [5]

7.4.1 Fixed Hydraulic Diameter

It was assumed that an elliptic pipe and the reference circular pipe (Table 7.1) have the same hydraulic diameter, which in the elliptic pipe was defined as $D_h = 4S/P_e = 25$ mm. Two basic dimensions of the ellipse a and b, shown in Fig. 7.7a, were assigned to be $a = D = D_h = 25$ mm and $b = 9.45$ mm. If the hydraulic diameter D_h remains unchanged, the elliptic area $S = \pi ab$, as compared to circular area $S = \pi a^2/4$, enlarged by a factor of $4b/a = 1.512$. As a result, the elliptic perimeter (representing the contact surface between the flow and the pipe) $P = 4S/D_h = 4S/a = 4\pi b$ also enlarged compared to the circular pipe perimeter $P = \pi D = \pi a$ by a factor of $4b/a = 1.512$. In a single pipe, the total mass flow rate was the same 0.0015 kg/s. The eccentricity parameter also remained unchanged $H = 82.5$ mm (Table 7.1).

Streamwise distributions of the local cross-sectional averaged Nusselt numbers and turbulence intensity in the elliptic pipes are plotted in Fig. 7.8a, b, c against

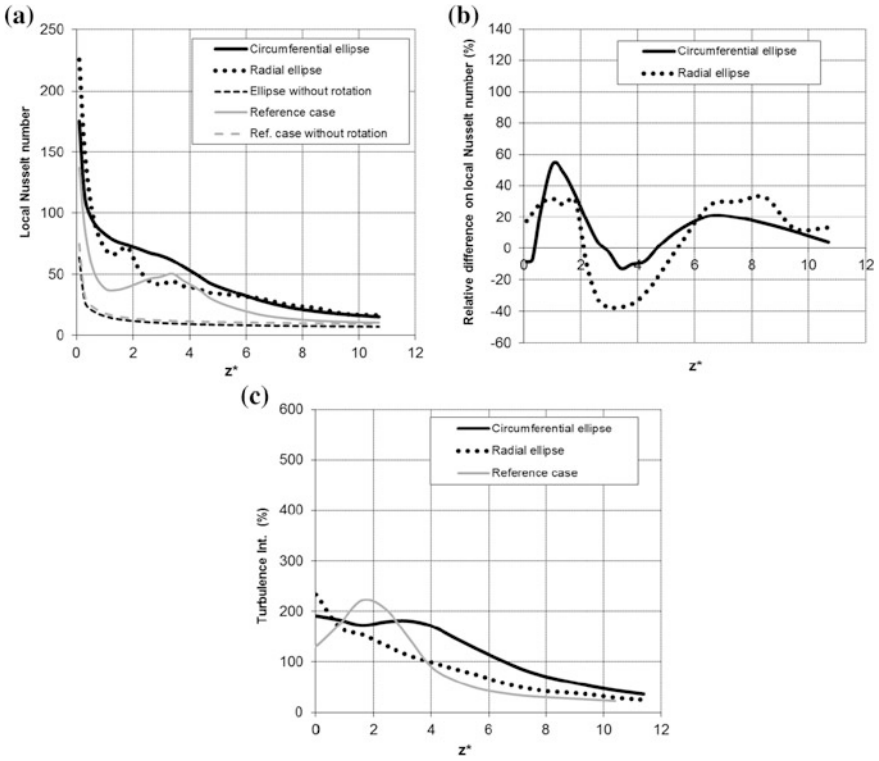

Fig. 7.8 Comparisons between the two ellipses and the reference case of the circular pipe, with the hydraulic diameter fixed: **a** local Nusselt numbers; **b** turbulence intensity; **c** relative difference from the reference case [5]

those in the reference circular pipe. It is evident that in elliptic pipes, the flow at $z^* > 9$ turns to be quasi-stabilized, which occurs at a larger distance from the inlet than in circular pipes. All curves flatten asymptotically to constant levels that are larger than those in circular pipes.

The functions of the local Nusselt numbers in Fig. 7.8a, c in both elliptic pipes look differently from those in the reference circular pipe. Next to the pipe inlet, the turbulence intensity is rather high (Fig. 7.8b). The highest turbulence intensity can be observed at $z^* > 3$ in the pipe with a circumferential elliptic cross section.

As mentioned above in the introduction, over the entrance length of a pipe, the radial and tangential velocities are rather large because of the initial flow swirl, which engenders large Coriolis forces.

Streamlines and temperature fields at the outlets of circumferential and radial elliptic pipes are shown in Figs. 7.7 and 7.9. Approaching the outlet of the elliptic rotating pipes flow turns to be quasi-stabilized and is accompanied with secondary flows caused by Coriolis forces. The nearly constant Nusselt number and turbulence intensity here are larger than those in stationary pipes. Mixing is better in the circumferential elliptic pipe (Fig. 7.7b), and air is in good contact with the pipe. On the contrary, three contra-rotating vortices emerge in the radial elliptic pipe with the middle vortex isolated (Fig. 7.7c). Therefore, air temperature fields are more uniform in Fig. 7.9a than in Fig. 7.9b, where air is involved in a closed circulation loop in the center of the channel. In the radial elliptic pipe, shear stresses are smaller due to the effects of three contra-rotating vortices [5].

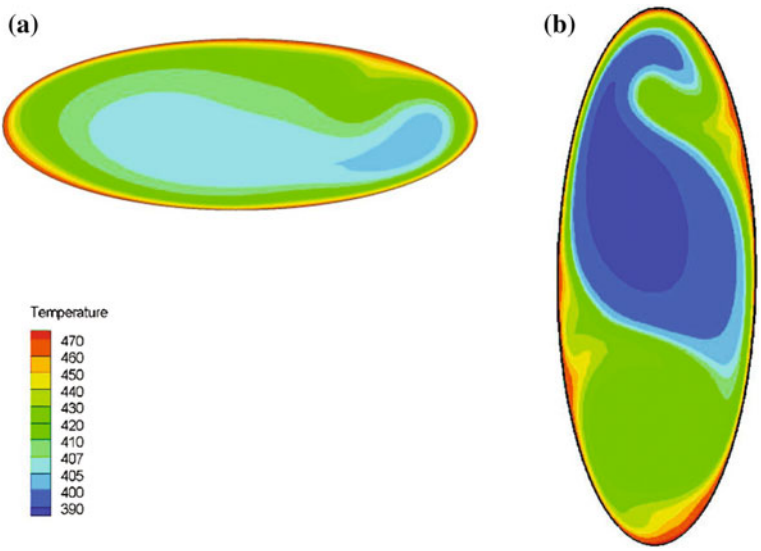

Fig. 7.9 Temperature distributions at the pipe outlet in elliptic pipes with the fixed hydraulic diameter: **a** circumferential pipe; **b** radial pipe [5]

Table 7.4 Cross-sectional geometry effect on heat transfer (hydraulic diameter fixed) [5]

	Mean *Nu*	Difference in *Nu* (%)	*h*	Contact surface *S*	$h \cdot S$	Difference in $h \cdot S$ (%)
Circular pipe	40.5	–	38.7	0.0224	0.87	–
Circumferential ellipse	44.5	+10	42.6	0.0338	1.44	+66.4
Radial ellipse	41.6	+2.8	39.7	0.0338	1.34	+54.8
Total heat transfer, 12 circular pipes			38.7	0.2688	10.40	–
Total heat transfer, 8 circumferential ellipses			42.6	0.2704	11.52	+10.8
Total heat transfer, 8 radial ellipses			39.7	0.2704	10.72	+3.1

As seen from Table 7.4, the mean Nusselt number increased in both circumferential and radial elliptic pipes in comparison with the circular reference pipe. However, the circumferential elliptic pipes increased the heat transfer by 10.0 %, i.e., more efficiently, than the radial elliptic pipes, which provide only 2.8 % heat transfer enhancement.

The overall heat transfer depends on a product of the heat transfer coefficient α and a channel surface *S* contacting the flow. In the case of an elliptic pipe, the contact surface is enlarged by 51.2 % as compared to the circular pipe. Hence, the product $\alpha \cdot S$ presented in Table 7.4 demonstrates 54.8–66.4 % increase in the radial and circumferential elliptic pipes, respectively, (compared to the circular pipe). This increase entails improvement of the entire cooling system efficiency.

However, the use of the elliptic pipes of the enlarged cross section instead of the circular pipes complicates their packaging in a motor in view of the necessity to ensure acceptable mechanical strength and electromagnetic flux distribution. As a result, only eight elliptic pipes can be installed in a real rotor instead of 12 circular pipes. Table 7.4 presents the data for overall amount of heat, in which cooling systems of 12 circular, 8 radial, and 8 circumferential elliptic pipes are able to remove from the rotor. As compared to the cooling system of 12 circular pipes, overall heat removal increases by only 3.1 % for the arrangement with 8 radial elliptic pipes and by 10.8 % for the configuration of 8 circumferential pipes. To remind, the mass flow rate $\dot{m} = 0.0015$ kg/s in a single elliptic pipe remained identical to that in the circular pipe. Thus, in the cooling configuration of 12 circular pipes, the total mass flow rate was $\dot{m} = 0.018$ kg/s in contrast to $\dot{m} = 0.012$ kg/s in the cooling configuration consisting of 8 elliptic pipes.

To correctly estimate the performance of the cooling configuration with 8 elliptic pipes, the overall mass flow rate through them must be enlarged also to $\dot{m} = 0.018$ kg/s, i.e., to $\dot{m} = 0.00225$ kg/s through a single pipe. Table 7.5 shows

Table 7.5 Heat transfer in the elliptic pipes with the increased mass flow rate $\dot{m} = 0.00225$ kg/s providing the same pressure drop [5]

	Mean $\overline{Nu}$	Difference in $\overline{Nu}$ (%)	α	Contact surface S	$\alpha \cdot S$	Difference in $h \cdot S$ (%)
Circumferential ellipse	53.3	+31.6	51	0.0338	6.05	+99.0
Radial ellipse	48	+18.5	45.9	0.0338	5.45	+79.3
Total mass flow rate, 8 circumferential ellipses			51	0.2704	13.8	+32.6
Total mass flow rate, 8 radial ellipses			45.9	0.2704	12.4	+19.3

that for the mass flow rate $\dot{m} = 0.00225$ kg/s in a single pipe, the heat transfer enhancement was 99 % in the circumferential and 79.3 % in the radial elliptic pipe in contrast to the circular pipe with $\dot{m} = 0.0015$ kg/s. The total cooling efficiency in the configuration with 8 elliptic pipes at $\dot{m} = 0.018$ kg/s (whose cumulative heat transfer surface is practically the same as that in the configuration of 12 circular pipes) is 32.6 % for circumferential and 19.3 % for radial elliptic pipes.

To recall, in an elliptic pipe, the cross-sectional area S is 1.512 times larger than that in a circular pipe. In view of the fact that the mass flow rate $\dot{m} = \rho \bar{V} S = 0.00225$ kg/s in an elliptic pipe is 1.5 times larger than $\dot{m} = 0.0015$ kg/s in a circular pipe, one can conclude that the mean axial velocity $\bar{V}$ is identical in both pipe geometries. Hence, the axial Reynolds number Re = 3500 is also identical, since the hydraulic diameter and the mean axial velocity remain the same. Therefore, one can expect that the pressure losses in a circular pipe with $\dot{m} = 0.0015$ kg/s must be equal to those in an elliptic pipe with $\dot{m} = 0.00225$ kg/s.

The Blasius equation for the friction factor for fully developed flow in stationary pipes valid for Re = 3000–100,000 [22]

$$f_0 = 0.316 Re^{-0.25} \tag{7.11}$$

delivers the value f = 0.041 for $\dot{m} = 0.0015$ kg/s. CFD simulations yield f = 0.047 for the stationary circular pipe with $\dot{m} = 0.0015$ kg/s, and f = 0.049 for the stationary elliptic pipe with $\dot{m} = 0.00225$ kg/s, which results in an only 4 % different value.

Thus, a calculation of the cooling system with 8 elliptic pipes having 51.2 % enlarged cross section disclosed the following disadvantages as compared to the reference configuration of 12 circular pipes: (a) reduced mechanical strength; (b) packaging problems, as elliptic pipes occupy locally more space; (c) larger nonuniformity of the circumferential temperature variation; and (d) deteriorated environment for magnetic flux circulation.

7.4.2 Fixed Equivalent Diameter

Drawbacks of the cooling configuration with 8 elliptic pipes mentioned above served as a motivation for an investigation of a cooling system with 12 elliptic pipes, whose cross-sectional area is identical to that of the reference circular pipe. This means keeping the equivalent diameter of the pipe $D_e = \sqrt{4S/\pi}$ unchanged and morphing it from a circular to an elliptic shape. Keeping in mind that the circular and the elliptic cross-sectional areas must be equal $S = \pi D^2/4 = \pi 0.025^2/4 = \pi ab$, the characteristic dimensions a and b of the ellipse (Fig. 7.7a) were chosen to be a = 16 mm and b = 9.77 mm.

Elliptic pipes were located circumferentially and radially, and the mass flow rate was set to be $\dot{m} = 0.0015$ kg/s. The elliptic cross section of the pipe being the same as that of a reference circular pipe provides a 6 % larger perimeter (i.e., the contact surface).

Figure 7.10a–c depicts functions of the local cross-sectional averaged Nusselt numbers in both elliptic pipes and the reference circular pipe. One can conclude

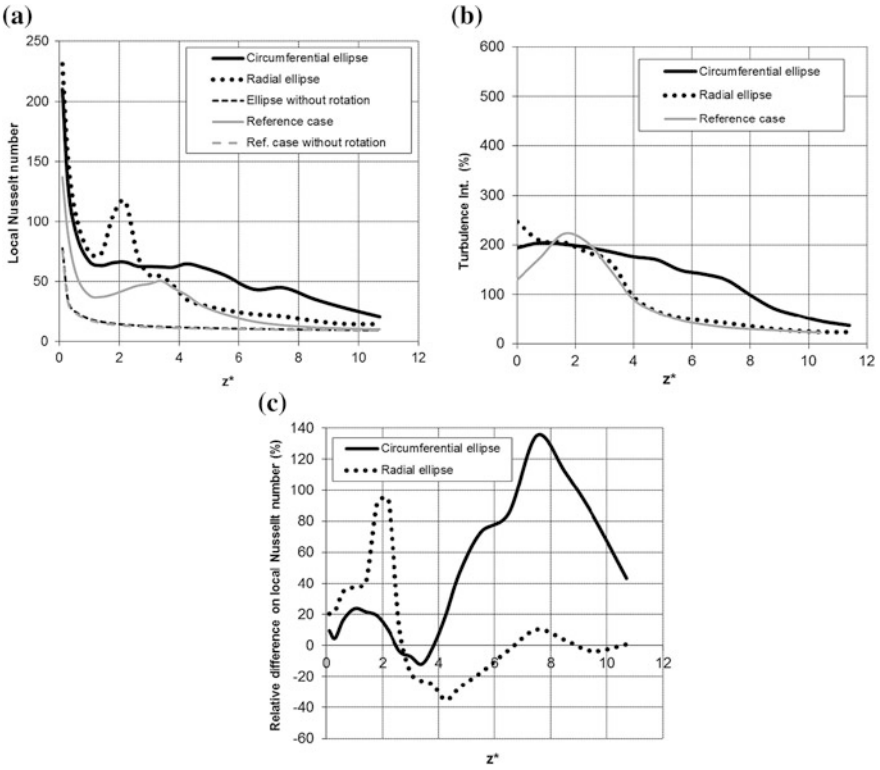

Fig. 7.10 Comparisons between two elliptic and reference circular pipes of the same equivalent diameter; **a** local Nusselt numbers; **b** turbulence intensity; **c** relative difference from the reference case [5]. Nusselt number is based on the equivalent diameter D_e

again that the higher turbulence intensity in the circumferential elliptic pipe ensures better performance than that in the radial elliptic pipe for $z^* > 2.7$. The Nusselt numbers level off to quasi-stabilized values near to the pipe outlet.

Path lines and temperature fields projected to the outlet of circumferential and radial elliptic pipes are shown in Figs. 7.11 and 7.12. Distinct secondary flows persist again over the span of the quasi-stabilized flow that sets on near to the outlet of the elliptic rotating pipes, which cause the Nusselt numbers and turbulence intensity to surpass those in non-rotating pipes though at a constant quasi-stabilized level.

Contrary to flow pattern in Fig. 7.7, only a single vortex in the cross sections of circumferential and radial elliptic pipes is visible in Fig. 7.11, because the cross-sectional shapes in Fig. 7.11 are closer to circular than those in Fig. 7.7.

In the circumferential elliptic pipe (Fig. 7.12a), the temperature field at the outlet cross section is more uniform than that of the vertical elliptic pipe (Fig. 7.12b), which is more symmetrically distributed than that in Fig. 7.9b. This phenomenon is apparently caused by the origin of a single vortex in Fig. 7.11b and three vortices in Fig. 7.7c.

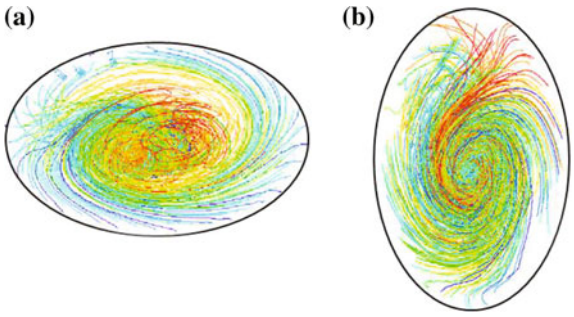

Fig. 7.11 Path lines at the pipe outlet of the elliptic pipes with the fixed equivalent diameter: **a** circumferential pipe; **b** radial pipe [5]

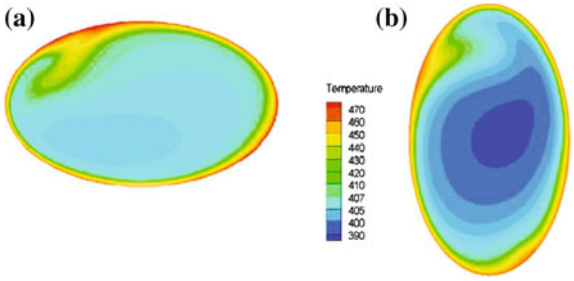

Fig. 7.12 Temperature distributions at the pipe outlet of elliptic pipes with the fixed equivalent diameter: **a** circumferential pipe; **b** radial pipe [5]

Table 7.6 Effect of a cross-sectional shape on heat transfer (equivalent diameter fixed) [5]

	Mean $\overline{Nu}$	Difference in $\overline{Nu}$ (%)	α	Contact surface S	$\alpha \cdot S$	Difference in $\alpha \cdot S$ (%)
Circular pipe	40.5	–	38.7	0.0224	0.87	–
Circumferential ellipse	52.5	+29.6	53.3	0.0237	1.26	+44.8
Radial ellipse	43.7	+7.9	44.3	0.0237	1.05	+20.7

Computations of the mean Nusselt number and the product of the heat transfer coefficient α and the wetted surface S are listed in Table 7.6 for the circular and both elliptic channels. With a fixed equivalent diameter, elliptic geometry brings larger improvement of heat transfer, than in the circular one.

A circumferential elliptic pipe displays again the best performance: 29.6 % enhancement of $\overline{Nu}$ and 44.8 % for the total cooling efficiency $\alpha \cdot S$. The radial elliptic pipe yields only 7.9 % enhancement of $\overline{Nu}$ and 20.7 % of $\alpha \cdot S$. The rate of enhancement of the total heat transfer $\alpha \cdot S$ in a single pipe stays in force also for the entire cooling configuration (as all of them consist of 12 pipes).

The pressure losses in the elliptic and circular pipe are the same, once the equivalent diameter and the mass flow rate do not change [22]. CFD simulations yield the friction factor of $f = 0.049$ in a non-rotating elliptic pipe for $\dot{m} = 0.0015$ kg/s (Table 7.7). This deviates from the value of $f = 0.047$ in a non-rotating circular pipe (Table 7.7) by 4 %. Thus, the pressure losses in the considered pipe geometries depend only on the mass flow rate.

From the point of view of the packaging, the cooling system configuration with 12 elliptic pipes, whose cross section has undergone only morphing and is equal to that of the reference circular pipes, is advantageous. These elliptic pipes can be installed in the same locations inside the real rotor, which helps to avoid the problems described above. To conclude, the use of elliptic pipes instead of the

Table 7.7 Calculated friction factors [5]

Configuration	Friction factor f
Stationary circular pipe ($\dot{m} = 0.0015$ kg/s)	0.047
Rotating circular pipe ($\dot{m} = 0.0015$ kg/s)	0.24
Fixed D_h, stationary ellipse ($\dot{m} = 0.0015$ kg/s)	0.060
Fixed D_h, rotating circumferential ellipse ($\dot{m} = 0.0015$ kg/s)	0.788
Fixed D_h, rotating radial ellipse ($\dot{m} = 0.0015$ kg/s)	0.516
Fixed D_h, stationary ellipse ($\dot{m} = 0.00225$ kg/s)	0.049
Fixed D_h, rotating circumferential ellipse ($\dot{m} = 0.00225$ kg/s)	0.408
Fixed D_h, rotating radial ellipse ($\dot{m} = 0.00225$ kg/s)	0.289
Fixed D_e, stationary ellipse ($\dot{m} = 0.0015$ kg/s)	0.049
Fixed D_e, rotating circumferential ellipse ($\dot{m} = 0.0015$ kg/s)	0.362
Fixed D_e, rotating radial ellipse ($\dot{m} = 0.0015$ kg/s)	0.276

circular pipes is beneficial in terms of the cooling system efficiency. From the technological point of view, the most efficient configuration is a *circumferential* elliptic pipe, whose *equivalent* diameter equals to that of a reference circular pipe.

7.4.3 Friction Factor in Rotating Pipes

Computed friction factors in circular and elliptic pipes of both types, rotating and non-rotating, are listed in Table 7.7. Based on these results, one can draw the following important conclusions.

It was proved above that the friction factor remained practically unchanged, once the cross section was subject to morphing (circular toward elliptic) and the axial Reynolds number (based on the hydraulic/equivalent diameter and average axial flow velocity) was kept identical $Re = 3500$: $f = 0.047$ for $\dot{m} = 0.0015$ kg/s in a non-rotating circular pipe, $f = 0.049$ for $\dot{m} = 0.00225$ kg/s in a non-rotating elliptic pipe with the same D_h and $f = 0.049$ for $\dot{m} = 0.0015$ kg/s in a non-rotating elliptic pipe with the same D_e.

In a non-rotating elliptic pipe with the same D_h and $\dot{m} = 0.0015$ kg/s, the friction factor exhibits an increased value $f = 0.06$, which can be explained in the following way. According to the Blasius Eq. (7.11), the friction factor f_0 (not the dimensional pressure losses) behaves as an increasing function for the decreased Reynolds number $Re = 2333$, which corresponds to the elliptic pipes with the same D_h and $\dot{m} = 0.0015$ kg/s. The friction factor is defined as $f = \Delta P D_h/(0.5\rho\bar{V}^2 L)$; for the compared cases, D_h and L are identical, while the ratio of the mean axial velocities $\bar{V}$ in the elliptic and circular pipe is 2333/3500 = 0.667 (Reynolds numbers are $Re = 2333$ and 3500, respectively). Hence, the ratio of the absolute pressure losses is $\Delta P_{Re=2333}/\Delta P_{Re=3500} = (0.06/0.047) \cdot 0.667^2 = 0.567$.

Table 7.7 shows that the friction factor drastically grows up in a rotating pipe. In a circular rotating pipe and $\dot{m} = 0.0015$ kg/s, the friction factor f is 5.1 larger as compared to a non-rotating pipe.

In elliptic pipes with the same D_h and unchanged Reynolds number $Re = 3500$ (in other words, for a larger cross section and $\dot{m} = 0.00225$ kg/s), the friction factor is 6.1 time larger in radial elliptic pipes and 8.7 times larger in circumferential elliptic pipes as compared to non-rotating circular pipes.

An analogous trend demonstrates elliptic pipes with the same D_e. In comparison with non-rotating circular pipes, the friction factor is 5.9 times larger for radial elliptic pipes and 7.7 times larger for the circumferential elliptic pipes.

To conclude, in a cooling system with 12 elliptic pipes obtained via morphing of the reference circular pipe and keeping the cross-sectional area unchanged, for the given Reynolds number $Re = 3500$ *more preferable circumferential elliptic pipes* ensured 45 % of the total heat transfer augmentation, which is the highest among all studied geometries. The friction factor in radial rotating elliptic pipes increased up to maximum 20 % larger than that in circular rotating pipes. Respective growth of

the friction factor in the circumferential rotating elliptic pipes was from 51 % (for the same D_e) to 70 % (for the same D_h) larger than that in circular rotating pipes. This confirms the tendency of the highest heat transfer augmentation exhibited by the circumferential elliptic rotating pipes. The heat transfer augmentation in rotating pipes is accompanied with the growth of the pressure losses. At the same axial Reynolds number and rotation rate, the circumferential elliptic rotating pipe for the same D_e exhibited a friction factor growth by 11.3 % smaller than that in the circumferential elliptic rotating pipe for the same D_h (in radial rotating elliptic pipes for the same D_e and the same D_h, this difference is equal to 4.4 %).

References

1. Chiu HC, Jang JH, Yan WM (2007) Combined mixed convection and radiation heat transfer in rectangular ducts rotating about a parallel axis. Int J Heat Mass Transfer 50(21–22): 4229–4242
2. Fasquelle A, Le Besnerais J, Harmand S, Hecquet M, Brisset S, Brochet P, Randria A (2010) Coupled electromagnetics acoustic and thermal-flow modeling of an induction motor of railway traction. Appl Therm Eng 30(17–18):2788–2795
3. Shevchuk IV, Khalatov AA (1996) Heat transfer and hydrodynamics in straight channels rotating about a parallel or inclined axis. High Temp 34(3):455–467
4. Sleiti AK, Kapat JS (2006) Heat transfer in channels in parallel-mode rotation at high rotation numbers. AIAA J Thermophys Heat Transfer 20(4):748–753
5. Fasquelle A, Pellé J, Harmand S, Shevchuk IV (2014) Numerical study of convective heat transfer enhancement in a pipe rotating around a parallel axis. Trans ASME J Heat Transfer 136(5):051901
6. Humphreys JF, Morris WD, Barrow H (1967) Convection heat transfer in the entry region of a tube which revolves about an axis parallel to itself. Int J Heat Mass Transfer 10(3):333–340
7. Morris WD (1981) Heat transfer and fluid flow in rotating coolant channels. Research Studies Press, J. Wiley and Sons
8. Baudoin B (1987) Contribution l'étude des conditions d'écoulement dans le circuit de refroidissement d'un moteur électrique de type ouvert. PhD thesis, Université de Poitiers, France
9. Borisenko AI, Dan'ko VG, Yakovlev AI (1974) Aerodinamika i Teploperedacha v Elekticheskikh Mashinakh (Aerodynamics and heat transfer in electrical machines). Energiya Publ, Moscow
10. Mahadevappa M, Rammohan Rao V, Sastri VMK (1996) Numerical study of steady laminar fully developed fluid flow and heat transfer in rectangular and elliptical ducts rotating about a parallel axis. Int J Heat Mass Transfer 39(4):867–875
11. Mori H, Shiobara R, Hattori K (2000) Heat transfer characteristic of a rectangular channel rotating on a parallel axis (1st report, study on flow and heat transfer characteristics of a large rotating electrical machine). Trans JSME Ser B 66(650):2650–2654
12. Morris WD, Woods JL (1978) Heat transfer in the entrance region of tubes that rotate about a parallel axis. J Mech Eng Sci 20(6):319–325
13. Morris WD, Dias FM (1980) Turbulent heat transfer in a revolving square-sectioned tube. J Mech Eng Sci 22(2):95–101
14. Stephenson PL (1984) An experimental study of flow and heat transfer in a duct, rotating about a parallel axis. Heat and mass transfer in rotating machinery. Hemisphere Publishing Corporation, Washington, DC, pp 39–49

15. Torii S, Yang WJ (1998) Thermal-fluid transport phenomena of a strongly-heated gas flow in parallel tube rotation. Int J Rotat Machinery 4(4):271–282
16. [FLUENT] ANSYS FLUENT User's Guide (2009) Version 12, ANSYS Inc
17. Kays WM, Crawford ME, Weigand B (2005) Convective heat and mass transfer, 4th edn. Mc-Graw-Hill, New York. ISBN: 0-07-246876-9
18. Jenkins SC, Shevchuk IV, von Wolfersdorf J, Weigand B (2012) Transient thermal field measurements in a high aspect ratio channel related to transient thermochromic liquid crystal experiments. Trans ASME J Turbomach 134 (3):031002
19. Jenkins SC, Zehnder F, Shevchuk IV, von Wolfersdorf J, Weigand B, Schnieder M (2013) The effect of ribs and tip wall distance on heat transfer for a varying aspect ratio two-pass ribbed internal cooling channel. Trans ASME J Turbomach 135(2):021001
20. Shevchuk IV, Jenkins SC, Weigand B, von Wolfersdorf J, Neumann SO, Schnieder M (2011) Validation and analysis of numerical results for a varying aspect ratio two-pass internal cooling channel. Trans ASME J Heat Transfer 133(5):051701
21. Çengel YA (1998) Heat transfer: a practical approach. WBC McGraw-Hill, New York
22. Munson BR, Young DF, Okiishi TH, Huebsch WW (2009) Fundamentals of fluid mechanics. Wiley, New York